Supporting Information

Low-Valent Iron: an Fe(I) Ate Compound as a Building Block for a Linear Trinuclear Fe Cluster

Crispin Lichtenberg[a,], Liliana Viciu[a], Matthias Vogt[a], Rafael E. Rodríguez-Lugo[a], Mario Adelhardt[b], Jörg Sutter[b], Marat M. Khusniyarov[b], Karsten Meyer[b], Bas de Bruin[c], Eckhard Bill[d], and Hansjörg Grützmacher[a,e]**

[a] Department of Chemistry and Applied Biosciences, ETH Zürich, CH-8093, Switzerland, hgruetzmacher@ethz.ch
[b] Department of Chemistry & Pharmacy, Friedrich-Alexander University, Erlangen - Nürnberg (FAU), Egerlandstr. 1, D-91058 Erlangen, Germany.
[c] Universiteit van Amsterdam, Faculty of Science, van 't Hoff Institute for Molecular Sciences Department of Homogeneous Catalysis, Postbus 94720, 1090 GS Amsterdam, The Netherlands.
[d] MPI für Chemische Energiekonversion, Stiftstr. 34-36, D-45470 Mülheim an der Ruhr, Germany.
[e] Lehn Institute of Functional Materials (LIFM), Sun Yat-Sen University, 510275 Guangzhou, China.

Experimental…… S02

Powder X-ray diffraction…… S06

Zero field Mössbauer spectroscopy…… S07

Magnetic susceptibility measurements…… S08

EPR spectroscopy and related DFT calculations…… S13

Cyclic voltammetry…… S14

[trop$_2$dad]…… S15

[FeBr$_2$(trop$_2$dad)] (**1**)…… S15

[Fe(trop$_2$dad)$_2$] (**4**)…… S16

Reaction of [Na(thf)$_3$Fe(trop$_2$dad)] (**2**) with Ph$_3$CCl…… S17

Ph$_3$CC$_6$H$_5$CPh$_2$ (**5**)…… S17

[Fe(trop$_2$dad-CPh$_3$)]·(Tol) (**6**)…… S18

Theoretical calculation of Mössbauer parameters…… S19

References…… S26

Experimental

General considerations.

All air- and moisture-sensitive manipulations were carried out using standard vacuum line Schlenk techniques or in an MBraun inert atmosphere dry-box containing an atmosphere of purified argon. C_6D_6, THF, THF-d_8, *n*-hexane, and toluene were distilled before use from sodium benzophenone ketyl or from sodium, respectively. CD_2Cl_2 was distilled before use from CaH_2. Naphtalene, sodium, CaH_2, Ph_3CCl and anhydrous $FeBr_2$ were obtained from Sigma Aldrich and used as received. NaH was obtained from sigma Aldrich as a dispersion in mineral oil and was washed with *n*-hexane and dried in vacuo prior to use. $Trop_2dad$, $[FeCl_2(thf)_{1.5}]$, $[FeBr_2(thf)_2]$, and $[Co(C_5H_5)_2]$ were synthesized according to the literature. NMR spectra were recorded on Bruker instruments operating at 200, 250, 300, or 500 MHz with respect to ^1H. ^1H NMR chemical shifts are reported relative to $SiMe_4$ using the residual ^1H chemical shifts of the solvent as a secondary standard. Infrared spectra were collected on a Perkin-Elmer-Spectrum 2000 FT-IR-Raman spectrometer. UV/vis spectra were recorded on UV/vis/NIR lambda-19-spectrometer in a cell with a 0.5 cm path length. Elemental analyses were performed at the Mikrolabor of ETH Zürich. Reliable elemental analysis data for **2** and **3** proved difficult to obtain due to the sensitivity of the samples. Alternative bulk methods of characterization are provided as evidence of the efficacy of the syntheses. Powder X-ray diffraction patterns of the samples were recorded with a STOE Stadi P diffractometer equipped with a germanium monochromator and CuKα1 radiation (operated at 35 mA, 35 kV). Powder spectra were simulated using WinXPow Version 3.0.1.13 (06-Dec-2010), STOE&Cie GmbH, 64295 Darmstadt, Germany. Single crystals suitable for X-ray diffraction were coated with polyisobutylene oil in a dry-box, transferred to a nylon loop and then transferred to the goniometer of an Oxford XCalibur diffractometer equipped with a molybdenum X-ray tube (λ = 0.71073 Å). The structures were solved using direct methods (SHELXS) completed by Fourier synthesis and refined by full-matrix least-squares procedures. Results from single crystal X-ray analysis are deposited as CCDC 1045323-1045329. ^{57}Fe Mössbauer spectra were recorded on a WissEl Mössbauer spectrometer (MRG-500) at 77 K in constant acceleration mode. ^{57}Co/Rh was used as the radiation source. WinNormos for Igor Pro software has been used for the quantitative evaluation of the spectral parameters (least-squares fitting to Lorentzian peaks). The minimum experimental line widths were 0.20 mm/s. The temperature of the samples was controlled by an MBBC-HE0106 MÖSSBAUER He/N_2 cryostat within an accuracy of ±0.3 K. Isomer shifts were determined relative to α-iron at 298 K. Experimental X-band EPR spectra were recorded on a Bruker EMX spectrometer (Bruker BioSpin) equipped with a He temperature control cryostat system (Oxford Instruments). Simulations of the EPR spectra were performed by iteration of the anisotropic *g*-values and line widths using the EPR simulation program W95EPR developed by Prof. Dr. Frank Neese. Magnetic susceptibility measurements were carried out with a superconducting quantum interference device (SQUID) magnetometer (Quantum Design, MPMS-5S) in the temperature range of 2-300 K in fields of 0.01 T and 1 T. Both field-cooled (FC) and zero-field-cooled (ZFC) data were obtained. For DFT calculations on compound **2** and related species ($[Fe(trop_2dad)]^-$, $[NaFe(trop_2dad)]$ and $[NaFe(trop_2dad)(thf)_3]$), the gas phase geometries were optimized with the Turbomole program package[1] coupled to the PQS Baker optimizer[2] via the BOpt package[3] at the unrestricted ri-DFT[4]/BP86[5] level. We used the def2-TZVP basis set[6] for all atoms and a small grid (m4). The minima (no imaginary frequencies) were characterized by calculating the Hessian matrix. The coordinates of the optimized geometries are supplied in a separated zip file (.pdb and .xyz format). EPR and Mössbauer parameters were calculated with the ORCA[7] program systems, using the coordinates from the structures optimized in Turbomole or the X-ray structure as input. For

the EPR parameters we used the b3-lyp[8] functional and the def2-TZVP basis set on all atoms. For the Mössbauer parameters we used the b3-lyp functional and the TZVP basis set on all atoms. The same method was applied for calculation of the Mössbauer parameters of **3** with Orca at the b3-lyp/TZVP level, but using the (non-optimized) geometry of the X-ray structure and employing the RIJCOSX approximation. The Mössbauer parameters of **3** were also computed using a different basis set combination, in particular using the CP(PPP) basis set on Fe. For these DFT calculations ORCA 2.7 revision 0 was used.[9] Again the geometry of **3** found in the crystal structure was used without geometry optimization. The single point calculations were performed with the B3LYP functional.[10] The "core-prop" (CP(PPP)) basis set for iron,[11] triple-ζ basis sets with one-set of polarization functions (TZVP) for nitrogen,[12] and double-ζ basis sets with one-set of polarization functions (SV(P)) for carbon and hydrogen atoms were used.[12] Mössbauer parameters were calculated as reported previously.[13] Spin density plots were visualized using the program Molekel.[14] Compounds **2**, **3**, **5**, and **6** were isolated as single crystals with solvent molecules in the lattice as described in the experimental part. If not otherwise noted, lattice bound solvent molecules were not or could not be removed under reduced pressure and yields refer to the compounds including the indicated amount of lattice bound solvents.

[$FeBr_2$(trop$_2$dad)] (1). Toluene (8 mL) was added to a mixture of trop$_2$dad (500 mg, 1.15 mmol) and [$FeBr_2(thf)_2$] (413 mg, 1.15 mmol). The reaction mixture turned green and was stirred at ambient temperature for 16 h. All volatiles were removed under reduced pressure to give a green solid which was dried in vacuo for 24 h. Yield: 748 mg, 1.15 mmol, quant.
Single crystalline material can be obtained by recrystallization from hot toluene or from CH_2Cl_2/hexanes (layering at ambient temperature).
^{1}HNMR (300 MHz, CD_2Cl_2): δ = –38.53 (br s, 2H), –3.21 (br s, 4H), 0.87 (br s, 4H), 3.18 (br s, 4H), 3.40 (br s, 4H), 5.98 (br s, 4H), 118.81 (br s, 2H) ppm. μ_{eff} = 4.7(1) μ_B (Evans' method). Anal. calc. for $C_{32}H_{24}N_2FeBr_2$ (652.21 g/mol): C, 58.93; H, 3.71; N, 4.30; found: C, 58.72; H, 3.60; N, 4.18. m.p. = 174 °C (decomp.). UV/VIS (THF): λ_{max} = 250, 652 nm. ATR IR: $\tilde{\nu}$ = 3019 (w), 2961 (w), 1599 (w), 1494 (w), 1436 (w), 1374 (w), 1307 (w), 1258 (s), 1085 (s), 1015 (s), 867 (w), 791 (s), 726 (s), 696 (w), 648 (w), 628 (w).

[$Na(thf)_3Fe$(trop$_2$dad)] · 0.5(C_6H_{14}) (2). Method A: Naphthalene (40 mg, 0.31 mmol) and sodium (22 mg, 0.96 mmol) were subsequently added to a stirred suspension of [$FeBr_2$(trop$_2$dad)] (200 mg, 0.31 mmol) in THF (4 mL). The reaction mixture turned brown and was filtered after 16 h. The filtrate was layered with hexanes (6 mL). Dark brown single crystalline needles of **2** formed within 20 h, were isolated by decantation and dried in a stream of Argon. A second crop of single crystalline material was obtained after 1 d upon cooling the mother liquor to –30 °C. Combined yield: 111 mg, 0.14 mmol, 45%. **Method B**: A suspension of NaH (83 mg, 3.46 mmol) in THF (1 mL) was added to a stirred suspension of [$FeBr_2$(trop$_2$dad)] (450 mg, 0.690 mmol) in THF (5 mL). The reaction mixture turned brown and a gas evolution was observed. After 2 h the reaction mixture was filtered and the filtrate layered with hexanes (20 mL). Dark brown single crystalline needles of **2** formed within 14 h, were isolated by decantation and dried in a stream of Argon. A second crop of single crystalline material was obtained after 1 d upon cooling the mother liquor to –30 °C. Combined yield: 392 mg, 0.506 mmol, 73%.
Only single crystalline material should be isolated in order to obtain material free of ferromagnetic and/or superparamagnetic impurities. Such impurities could only be detected

by magnetic susceptibility measurements. Contaminated samples showed effective magnetic moments of up to 9.7 μ_B.
^{1}HNMR (300 MHz, THF-d_8): δ = –1.02 (br s), 0.07 (br s), 7.26 (br s), 15.76 (br s) ppm. Resonances for THF and hexanes were also detected. m.p. > 220 °C. ATR IR: $\tilde{\nu}$ = 3058 (w), 2972 (m), 2868.94 (m), 1591 (m), 1508 (w), 1477 (s), 1455 (s), 1380 (m), 1361 (m), 1333 (w), 1299 (m), 1272 (w), 1258 (m), 1197 (m), 1179 (m), 1147 (m), 1121 (w), 1047 (s), 971 (w), 887 (s), 852 (m), 825 (m), 798 (m), 747 (s), 738 (s), 725 (s), 707 (s), 673 (m), 657 (s), 626 (s) cm^{-1}. UV/VIS (THF): λ_{max} = 237, 279, 306, 436 nm. Zero-field ^{57}Fe Mössbauer (δ, $|\Delta E_Q|$ (mm/s)): (77 K) 0.21(1), *2.45(1)* (Γ_{FWHM} = 0.33(1) mm/s). μ_{eff} = 1.80 μ_B (300 K, SQUID magnetometry, 0.01 T). μ_{eff} = 1.9(1) μ_B (298 K, Evans' method, 300 MHz NMR).

[Fe$_3$(trop$_2$dad)$_2$] · ((THF)$_{0.6}$(Hexanes)$_{0.2}$) (3). Method A: [FeCl$_2$(thf)$_{1.5}$] (22 mg, 94 µmol) was added to a solution of [Na(thf)$_3$Fe(trop$_2$dad)] (**2**) (148 mg, 191 µmol) in THF (3 mL). The reaction mixture was filtered after 1 h and the filtrate layered with hexanes (8 mL). Deep red-brown single crystalline plates of **3** had formed after 14 h, were isolated by decantation and dried in a stream of argon. Yield: 85 mg, 77 µmol, 82%. **Method B**: [Na(thf)$_3$Fe(trop$_2$dad)] (**2**) (144 mg, 186 µmol) was added to a solution of FeBr$_2$ (20 mg, 93 µmol) in THF (3 mL). The reaction mixture was filtered after 1 h and the filtrate layered with hexanes (6 mL). Deep red-brown single crystalline plates of **3** had formed after 16 h, were isolated by decantation and dried in a stream of argon. Yield: 76 mg, 69 µmol, 74%.
Only single crystalline material should be isolated in order to obtain material minimized in the content of ferromagnetic and/or superparamagnetic impurities. Such impurities could only be detected by magnetic susceptibility measurements. Contaminated samples showed effective magnetic moments of up to 10.7 μ_B. Method B proofed to be slightly more reliable in this respect.
^{1}H NMR (300 MHz, C_6D_6): δ = –37.26 (s), –31.54 (s), –26.48 (s), –18.18 (s), –8.41 - –4.63 (m), 8.70-10.79 (m), 12.52-14.17 (m), 22.92 (s), 27.45 (s), 54.21 (s), 55.97 (s), 76.36 (s), 123.51 (s) ppm. Resonances for THF and hexanes were also detected. m.p. > 220 °C. μ_{eff} = 6.00 μ_B (300 K, SQUID magnetometry, 1 T). μ_{eff} = 5.4(2) μ_B (Evans' method, 298 K, 300 MHz, 1.5·10^{-3} molar solution of **3** in C_6D_6, corrected for diamagnetic contribution and TIP contribution as obtained from fit of SQUID data). ATR IR: $\tilde{\nu}$ = 3054 (w), 2951 (w), 2923 (w), 2852 (w), 1595 (m), 1568 (w), 1481 (s), 1458 (s), 1382 (m), 1338 (w), 1317 (w), 1296 (m), 1250 (m), 1214 (w), 1195 (m), 1174 (w), 1156 (m), 1138 (w), 1121 (m), 1108 (w), 1069 (w), 1035 (w), 985 (w), 932 (m), 899 (m), 885 (m), 866 (m), 800 (w), 779 (w), 734 (s), 701 (w), 658 (w) cm^{-1}. UV/VIS (THF): λ_{max} = 225, 275, 449 nm. Zero-field ^{57}Fe Mössbauer (δ, $|\Delta E_Q|$ (mm/s)): (77 K) component 1 (68%): 0.37(1), *1.09(1)* (Γ_{FWHM} = 0.33(1) mm/s); component 2 (32%): 0.92(1), *1.88(1)* (Γ_{FWHM} = 0.24(1) mm/s).

[Fe(trop$_2$dad)$_2$] (4). [Co(C$_5$H$_5$)$_2$] (29 mg, 153 µmol) was added to a suspension of [FeBr$_2$(trop$_2$dad)] (50 mg, 77 µmol) and trop$_2$dad (33 mg, 76 µmol) in toluene (4.5 mL). After 3 h the reaction mixture was filtered. The filtrate was layered with hexanes (11 mL) and stored at –30°C. After 3 d dark brown single crystals had formed which were filtered off and dried in vacuo. The filtrate was layered with hexanes (6 mL) and stored at –30°C. After 2 d a second crop of single crystalline material had formed, which was isolated by filtration and dried in vacuo. Combined yield: 26 mg, 28 µmol, 36%.

^{1}H NMR (300 MHz, C_6D_6): δ = 5.26 (br s, 4H, H^{Benzyl}), 6.14-9.04 (br m, 22H, $H^{Olefin,Arom}$) ppm. m.p. = 179 °C (decomp.). μ_{eff} = 2.6(1) μ_B (Evans' method). UV/VIS (THF): λ_{max} = 220, 284, 463 nm. ATR IR: $\tilde{\nu}$ = 3016 (w), 2856 (w), 1628 (w), 1597 (w), 1483 (m), 1456 (m), 1436 (m), 1337 (w), 1307 (w), 1247 (w), 1209 (m), 1158.37 (w), 1105 (w), 1061 (m), 1035 (m), 971 (w), 948 (w), 886 (w), 829 (w), 795 (s), 766 (s), 735 (s), 652 (m), 642 (m) cm^{-1}. $C_{64}H_{48}N_4Fe$ (928.96 g/mol): C, 82.75; H, 5.21; N, 6.03; found: C, 82.67; H, 5.30; N, 6.11.

Reaction of [Na(thf)$_3$Fe(trop$_2$dad)] with Ph$_3$CCl. Ph_3CCl (29 mg, 104 µmol) was added to a stirred suspension of **2** (81 mg, 105 µmol) in THF (2 mL). After 5 h the reaction mixture was filtered. The filtrate was layered with hexanes (8 mL) and cooled to –30°C to give single crystalline colorless **5** after 3 d, which was filtered off and dried in a stream of Argon (11 mg, 19 µmol, 37% with respect to Ph_3CCl).
The filter cake was extracted with toluene (2 × 1 mL) and filtered. The filtrate was layered with hexanes (8 mL) to give single crystalline **3** after 1 d, which was filtered off and dried in a stream of Argon (14 mg, 13 µmol, 37% with respect to Fe).
The toluene/hexanes filtrate was stored at ambient temperature for 21 d to give dark brown single crystalline **6**, which was filtered off and dried in a stream of Argon (9 mg, 11 µmol, 11%).

Ph$_3$CC$_6$H$_5$CPh$_2$ · (C$_6$H$_{14}$) (5).[15] ^{1}H NMR (200 MHz, C_6D_6) δ = 4.92 (tt, $^3J_{HH}$ = 3.8 Hz, $^4J_{HH}$ = 2.0 Hz, 1H, H^{aliph}), 5.92 (dd, $^3J_{HH}$ = 10.5 Hz, $^3J_{HH}$ = 3.8 Hz, 2H, H^{olefin}), 6.44 (dd, $^3J_{HH}$ = 10.5 Hz, $^4J_{HH}$ = 2.0 Hz, 2H, H^{olefin}), 6.95-7.11 (m, 20H, H^{arom}), 7.28-7.31 (m, 5H, H^{arom}) ppm.
[Fe(trop$_2$dad-CPh$_3$)]·(Tol) (6). ^{1}H NMR (300 MHz, C_6D_6): δ = –2.73 (br s), –1.27 (br s), 1.65 (br s), 2.35 (br s), 3.75 (br s), 4.29 (br s), 6.00 (br s), 6.03 (br s), 6.12 (br s), 6.50 (br s), 6.61 (br s), 8.20 (br s), 24.74 (br s), 29.03 (br s) ppm. m.p. = 215 °C (decomp.). UV/VIS (THF): λ_{max} = 216, 276, 468 nm. ATR IR: $\tilde{\nu}$ = 3058 (w), 3019 (w), 2971 (w), 2920 (w), 1595 (w), 1560 (w), 1483 (m), 1463 (m), 1443 (m), 1397 (w), 1344 (w), 1297 (m), 1264 (w), 1184 (m), 1158 (w), 1123 (w), 1099 (w), 1033 (m), 1002 (w), 964 (w), 935 (w), 914 (w), 884 (w), 863 (w), 804 (w), 794 (w), 763 (w), 750 (s), 731 (s), 712 (m), 699 (s), 667 (s), 625 (m) cm^{-1}. μ_{eff} = 1.9(1) μ_B (Evans' method). $C_{58}H_{47}N_2Fe$ (827.87 g/mol): C, 83.94; H, 5.72; N, 3.38; found: C, 84.15; H, 5.60; N, 3.11.

Powder X-ray diffraction.

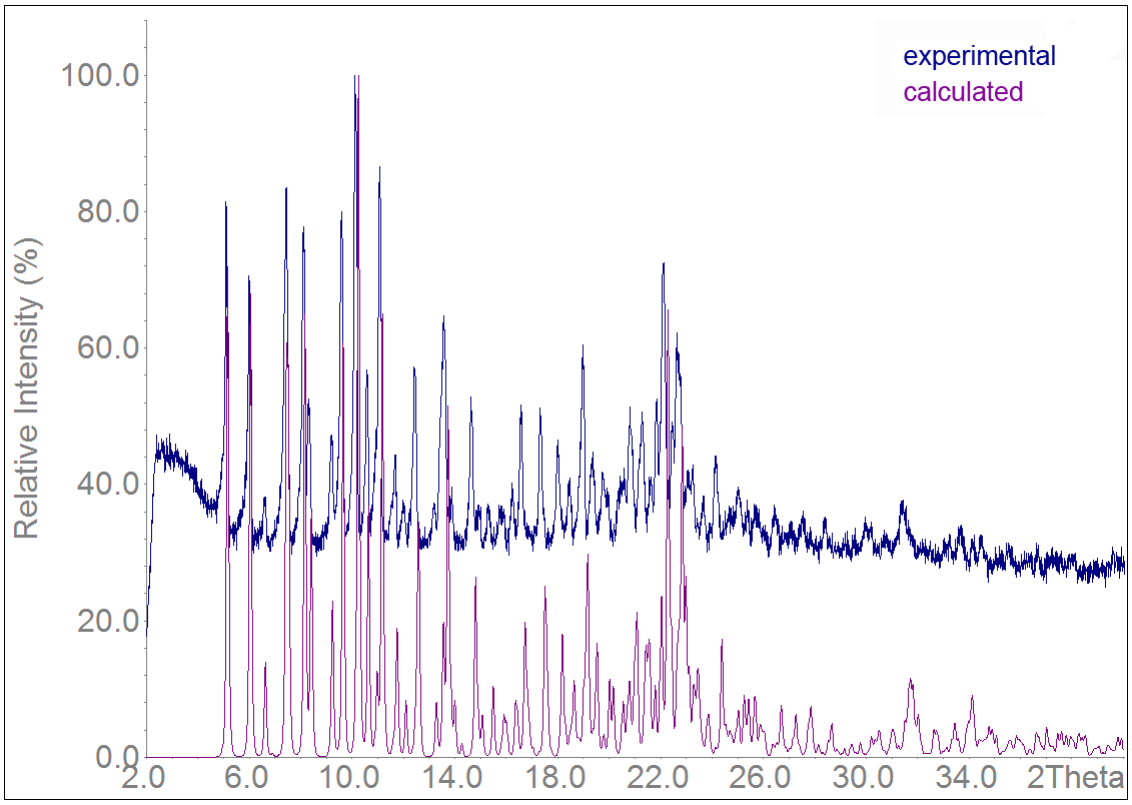

Figure S1. Experimental (blue) and calculated (magenta) X-ray powder diffractogram for [NaFe(trop$_2$dad)(thf)$_3$] (**2**) at room temperature.

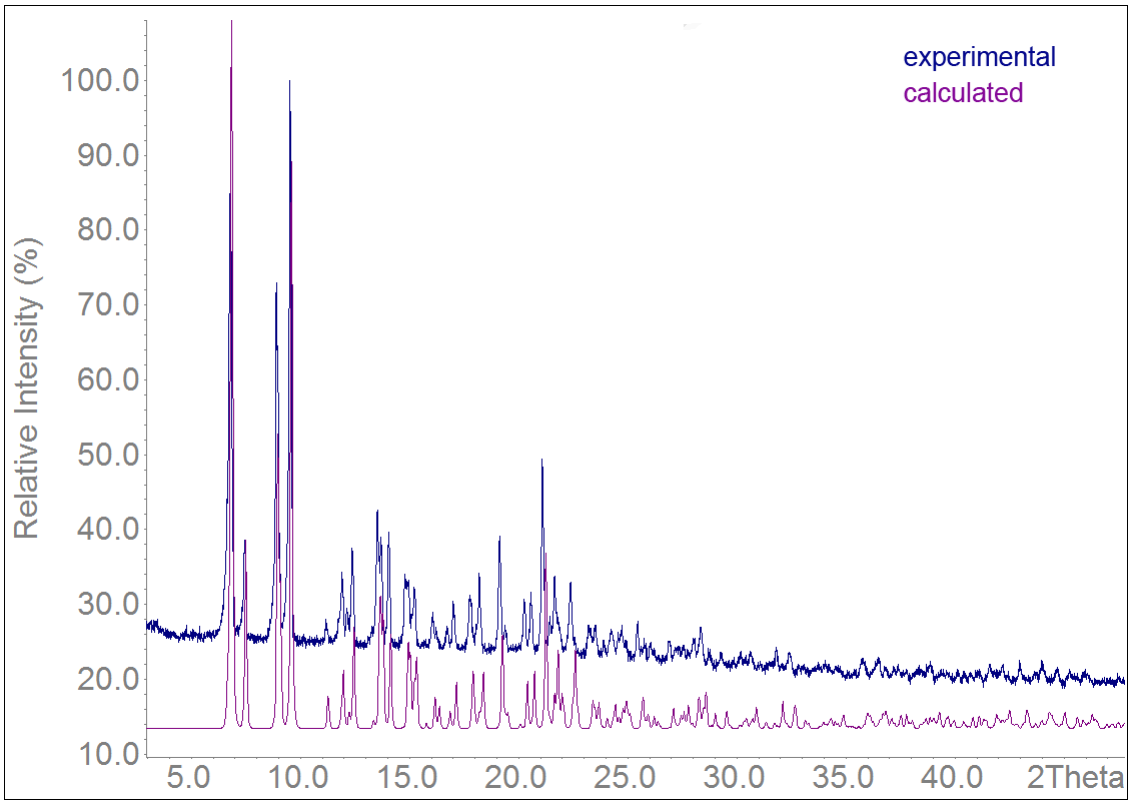

Figure S2. Experimental (blue) and calculated (magenta) X-ray powder diffractogram for [Fe$_3$(trop$_2$dad)$_2$] (**3**) at room temperature.

Zero field Mössbauer spectroscopy.

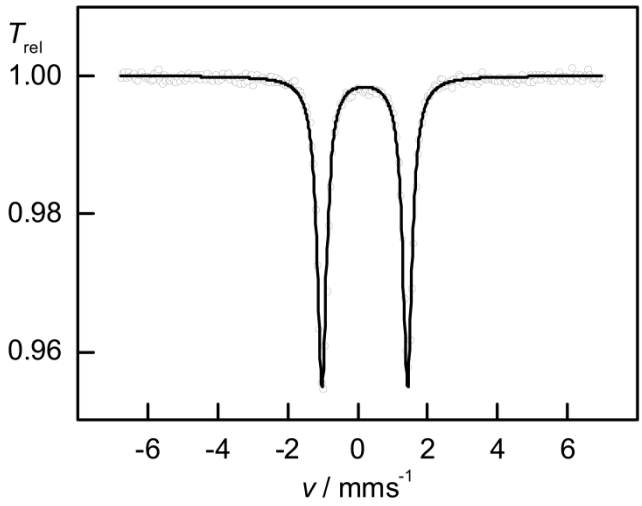

Figure S3. Zero field Mössbauer spectrum of [NaFe(trop$_2$dad)(thf)$_3$] (**2**) at 77 K. δ = 0.21(1) mm/s; $|\Delta E_Q|$ = 2.45(1) mm/s; Γ_{FWHM} = 0.33(1) mm/s.

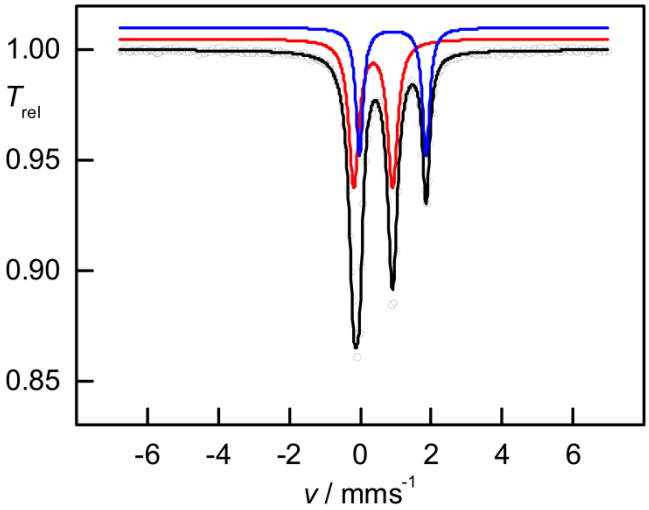

Figure S4. Zero field Mössbauer spectrum of [Fe$_3$(trop$_2$dad)$_2$] (**3**) at 77 K. Measured spectrum shown in black; subspectrum 1 (red, relative area: 68%); δ = 0.37(1) mm/s; $|\Delta E_Q|$ = 1.09(1) mm/s; Γ_{FWHM} = 0.33(1) mm/s; subspectrum 2 (blue, relative area: 32%); δ = 0.92(1) mm/s; ΔE_Q = 1.88(1) mm/s; Γ_{FWHM} = 0.24(1) mm/s.

Magnetic susceptibility measurements.

The temperature dependence of the magnetic susceptibility and magnetic moment of **2** are shown in Figure S5. **2** behaves paramagnetically in the whole temperature range. The data were fitted with the Curie Weiss law $(\chi - \chi_0) = (8(C/(T - \theta))T)^{½}$ after the diamagnetic contribution ($\chi_0 = -9.0(3)\cdot10^{-5}$) was subtracted. The Curie constant $C = 0.4016(1)$ and the Weiss constant $\theta = -0.028(3)$ K were obtained from the fit. A magnetic moment of $\mu_{eff} = 1.80$ μ_B is observed in the temperature range of 3-300 K. The moment is consistent with S = 1/2 for Fe(I) and coresponds to a low spin d^7 configuration ion. No field dependence on the magnetic moment was detected (see inset in Figure S5). This rules out the presence of superparamagnetic impurities.

The relation

$$\mu_{eff} = g_{average} \cdot \sqrt{S \cdot (S+1)}$$

gives an average g value of 2.08 for compound **2** based on magnetic susceptibility measurements. This is in good agreement with the geometric average of the g values determined by EPR spectroscopy, $g_{average} = 2.10$, and rules out the presence of ferromagnetic or paramagnetic impurities.

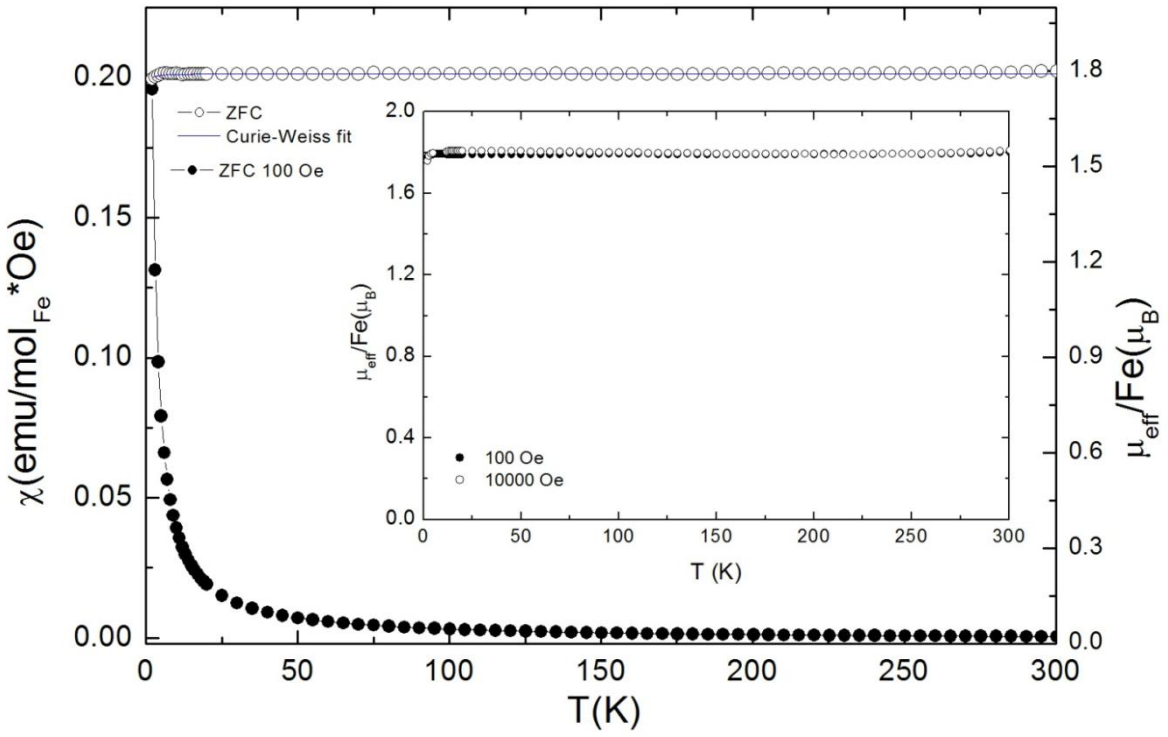

Figure S5. Temperature dependence of magnetic susceptibility for **2**. The magnetic moment dependence on temperature is also shown with the blue line representing the Curie Weiss fit (see text). The inset shows the effective magnetic moment at 0.01 T and at 1 T.

Magnetic susceptibility data of microcrystalline[16] **3** were recorded in the range of 2-300 K in applied fields of 0.01 T and 1 T (Figure S6-8).

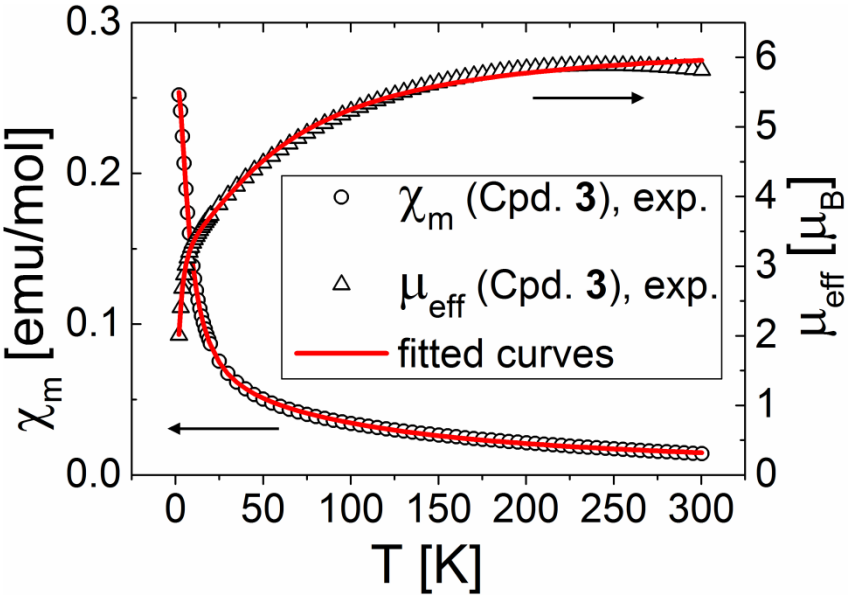

Figure S6. Temperature dependence of molar magnetic susceptibility (circles) and effective magnetic moment (triangles) of $[Fe_3(trop_2dad)_2]$ (**3**) (red lines indicate fits (see text)).

The data were analyzed using the program JulX by Dr. Eckhard Bill. The data obtained at 1 T was in good agreement with a spin Hamiltonian model for local spins $S_{Fe1} = S_{Fe3} = 1/2$, $S_{Fe2} = 2$ with the following parameters:

$J_{Fe1Fe2} = J_{Fe2Fe3} = -10.0$ cm^{-1}, $J_{Fe1Fe3} = -23.0$ cm^{-1},
$g_{Fe1} = g_{Fe3} = 2.79$, $g_{Fe2} = 2.17$,
$D_{Fe2} = -46.2$ cm^{-1}, $E_{Fe2}/D_{Fe2} = 0.31$,
diamagnetic correction: $-578.5 \cdot 10^{-6}$ emu.

A large zero field splitting parameter D_{Fe2} was chosen as a starting point in the simulations due to the wide split subspectrum of Fe2 in the applied field Mössbauer spectrum of **3**, which seems to indicate large magnetic anisotropy due to sizable zero-field splitting. The latter can arise only from Fe2 because the terminal Fe(I) ions are in doublet state and, hence, cannot contribute single-ion zero-field splitting. The applied field Mössbauer data are not discussed here in detail, because a fully consistent global spin Hamiltonian simulation could not yet be obtained due to the complexity of the spin ladder and related spin relaxation issues, arising from competing moderately strong all-antiferromagnetic spin coupling and a pronounced local zero field splitting of $S_{Fe2} = 2$ in compound **3**.

It should be mentioned that an acceptable fit of the magnetic susceptibility data could also be obtained using the above model with other parameters. The error plots in Figure S7 indicate possible solutions.

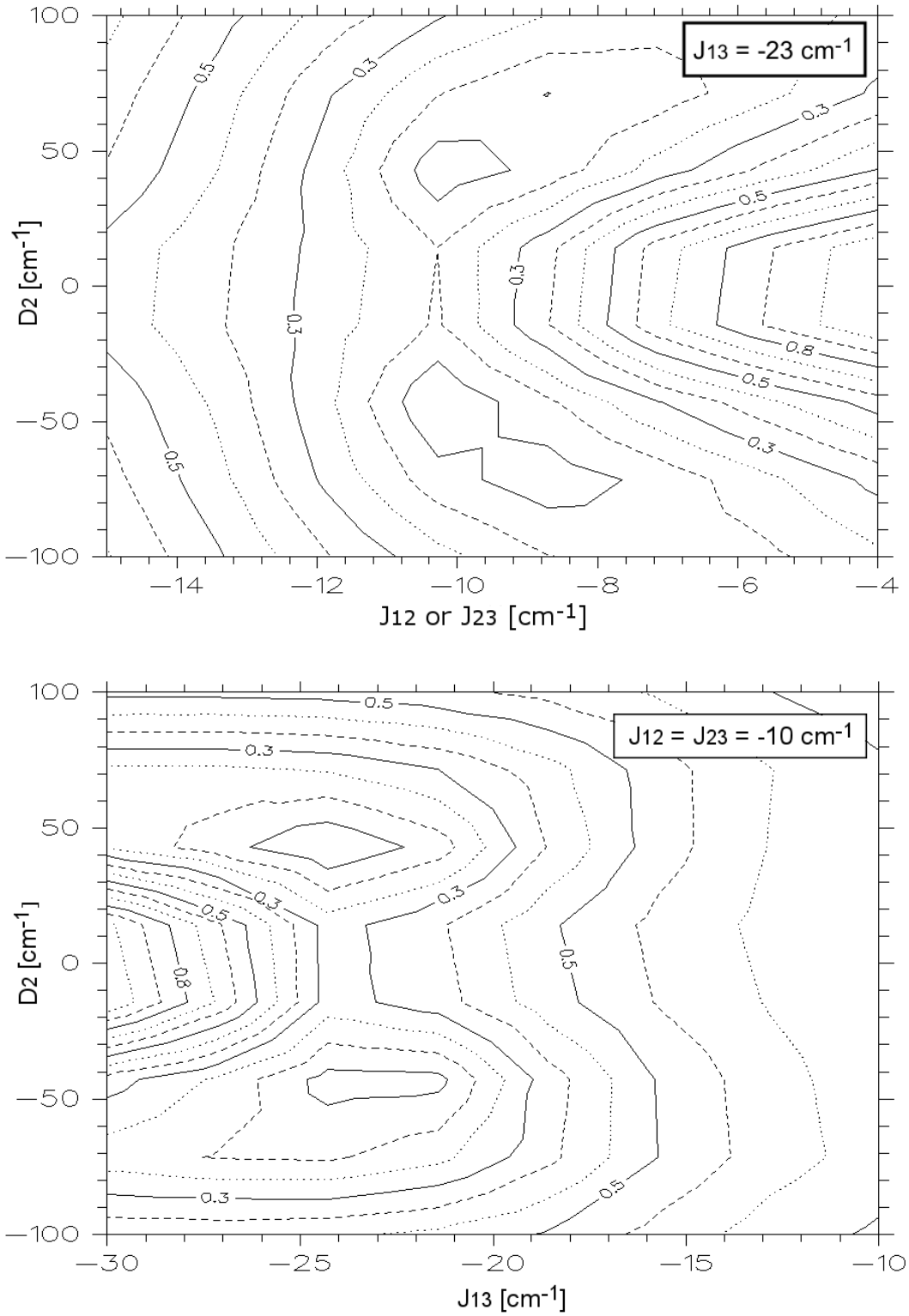

Figure S7. Top: error plot for D_2 vs J_{12} (where $J_{12} = J_{23}$). Bottom: error plot for D_2 vs. J_{13}. Parameters used are those given on page S09.

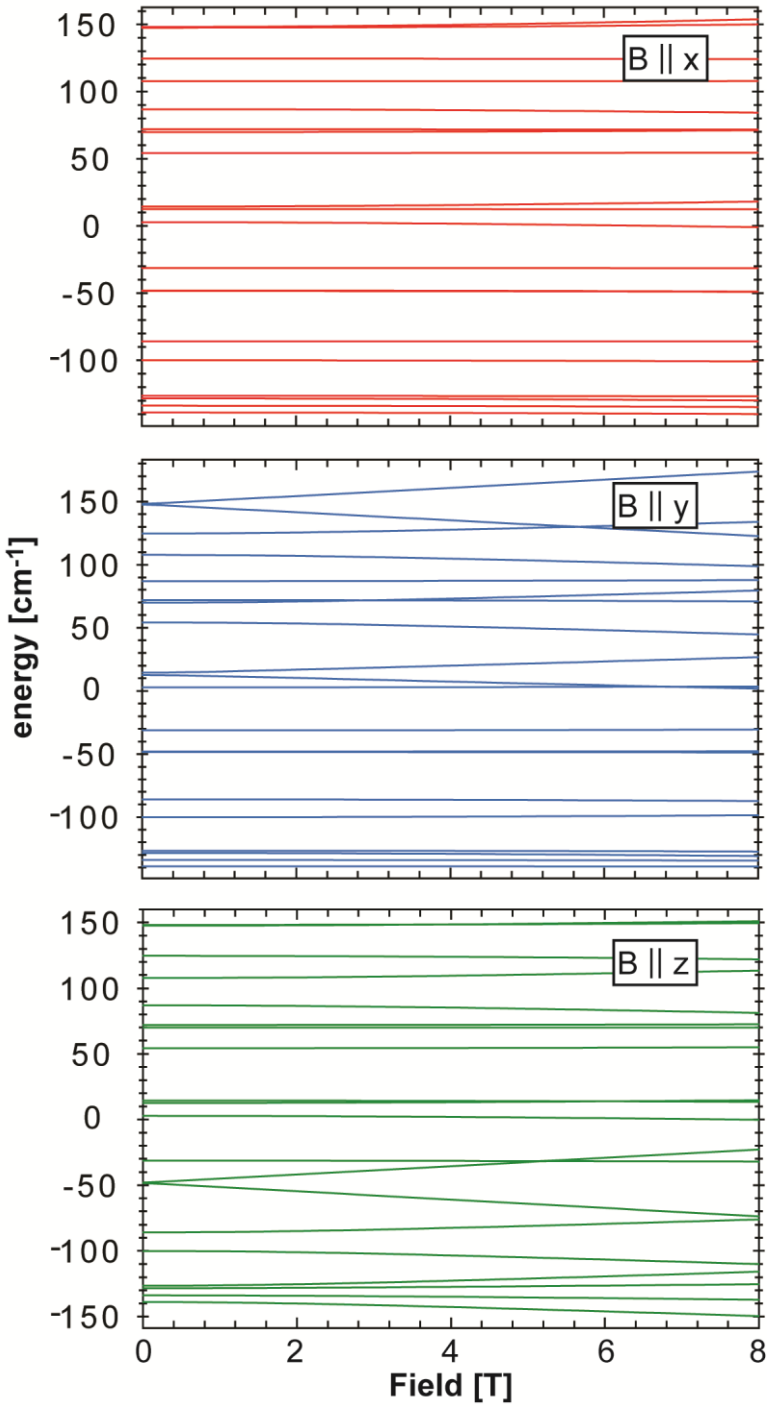

Figure S8. Energy plot of the magnetic eigenstates for **3** vs. a field applied in x-, y-, and z-direction with respect to the magnetic axes defined by the zero-field splitting tensor of Fe2.

At a low applied field of 0.01 T a higher effective magnetic moment was obtained (μ_{eff} = 5.8 μ_B at 300 K and 1 T; μ_{eff} = 6.4 μ_B at 300 K and 0.01 T (corrected only for diamagnetic contribution)).[17] At low temperatures and an applied field of 0.01 T, a transition is apparent in the ZFC data at 5 K while the FC curve diverges from the ZFC curve (Figure S9). The observed behavior is most likely due to the presence of small amounts of superparamagnetic impurities, although it cannot strictly be excluded to be an intrinsic property of compound **3** in solid state.[18] Extensive electronic and magnetic studies are required to clarify the type of interactions in **3** in low magnetic fields, ideally on single crystals and would be beyond the scope of this communication.

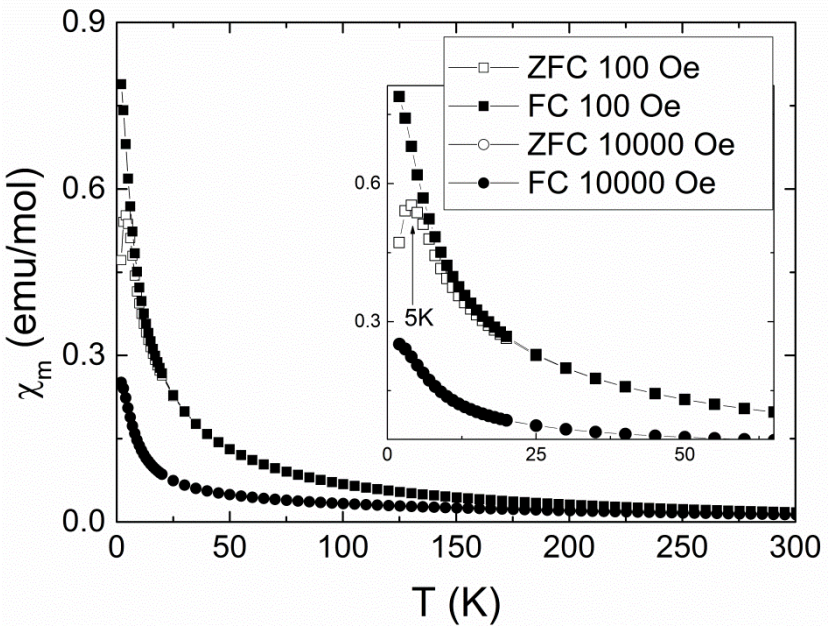

Figure S9. Temperature dependence of molar magnetic susceptibility at 0.01 T and 1 T for **3** (ZFC and ZFC data are shown, data corrected only for diamagnetic contribution).

EPR spectroscopy. The X-band EPR spectrum of [NaFe(trop$_2$dad)(thf)$_3$] (**2**) shown in Figure 1b (main part) was recorded at 20 K in frozen THF /0.1 M [N(*n*Bu)$_4$][PF$_6$]. Experimental conditions: microwave power 0.2 mW, field modulation amplitude = 2 Gauss, microwave frequency = 9.368145 GHz. The simulated spectrum was obtained with the parameters shown in Table S1. Spin density and SOMO plots of the [Fe(trop$_2$dad)]$^-$ anion are shown in Figure S10 revealing a mainly d_{Z^2} type topology for the SOMO.

Table S1. Experimental and DFT calculated *g*-values and DFT calculated Fe spin densities of [NaFe(trop$_2$dad)(thf)$_3$)] (**2**) and related species.[(a),(b)]

Exp. (simulation)	g_x	g_y	g_z	**spin density Fe** [(a)]	**NBO charge Fe** [(a)]
[NaFe(trop$_2$dad)(thf)$_3$] (**2**)	2.010	2.095	2.199	-	-
DFT [(a), (b)]	g_x	g_y	g_z	**spin density Fe** [(a)]	**NBO charge Fe** [(a)]
[Fe(trop$_2$dad)]$^-$ *free anion*	2.022	2.080	2.117	1.35	0.659
[NaFe(trop$_2$dad)]	2.022	2.083	2.134	1.23	0.574
[NaFe(trop$_2$dad)(thf)$_3$] *DFT geom.*				1.33	0.636
[NaFe(trop$_2$dad)(thf)$_3$] *X-ray geom.*[(c)]	2.021	2.078	2.136	-	-

(a) Geometry of the [Fe(trop2dad)]$^-$ anion, optimized in the gas phase with Turbomole (BP86, def2-TZVP).

(b) EPR parameters calculated with Orca (b3-lyp, def2-TZVP) using the Turbomole optimized geometries.

(c) Geometry found in the X-ray structure, not optimized with DFT; using geometries of asymmetric units 1 or 2 gave identical *g*-values.

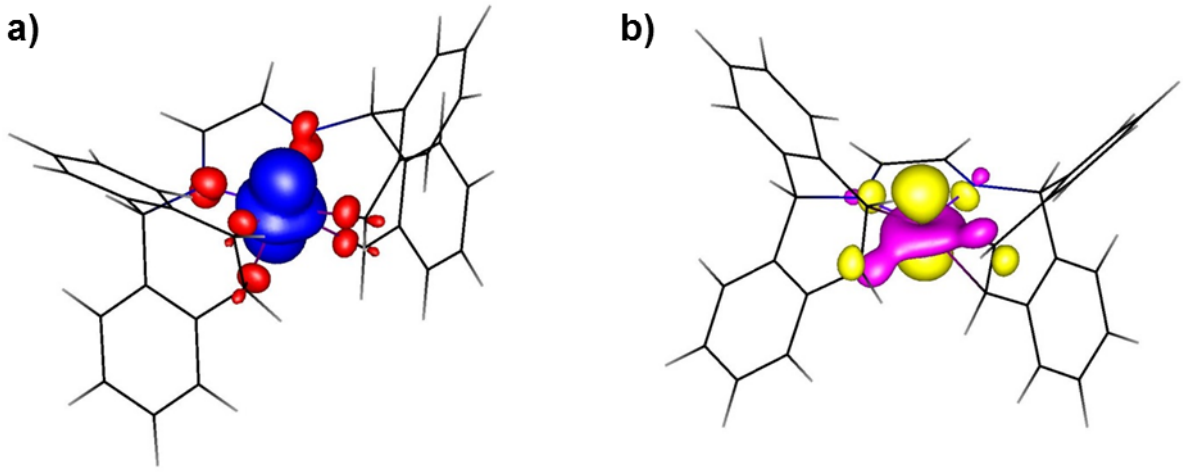

Figure S10. Spin density (a) and SOMO (b) plots of the [Fe(trop$_2$dad)]$^-$ anion.

The X-band EPR spectrum of $[Fe_3(trop_2dad)_2]$ (**3**) recorded in toluene solution at room temperature shows a broad featureless signal (Figure S11a). At 20 K in a toluene glass, an even broader featureless signal is observed, which extends over the full magnetic field sweep (Figure S11b). This is characteristic of small, mostly single-domain magnetic particles, the anisotropy of which determines the width of their (ferro)magnetic resonance spectrum. Their line width *decreases* with increasing temperatures, unlike for paramagnetic systems, because the effective magnetic anisotropy decreases when the barrier can be thermally crossed. (this effect is size dependent and more pronounced for smaller particles).[19] Thus, the X-band EPR signal observed in samples of **3** was assigned to small magnetic particles, which are present as minor impurities or form upon beginning decomposition of **3** in solution.

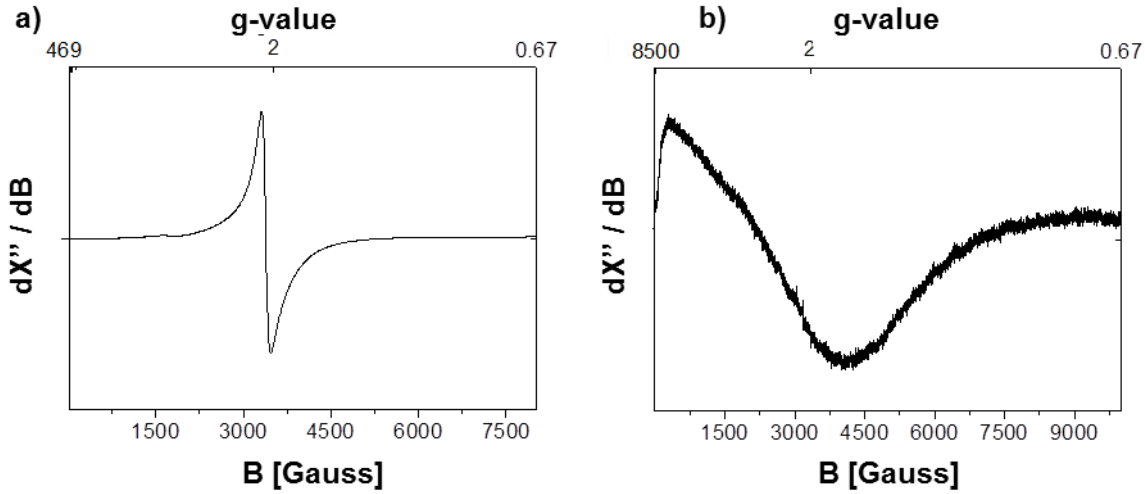

Figure S11. X-band EPR spectra of $[Fe_3(trop_2dad)_2]$ (**3**) in a toluene solution at room temperature (a) and in a toluene glass at 20 K (b). Experimental conditions: a) microwave power 2.007 mW, field modulation amplitude = 10 Gauss, microwave frequency = 9.86533 GHz. b) microwave power 0.632 mW, field modulation amplitude = 2 Gauss, microwave frequency = 9.369638 GHz.

Cyclic voltammetry.

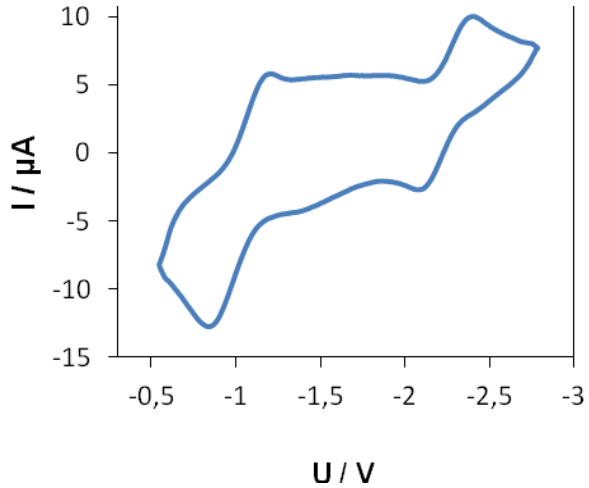

Figure S12. Cyclic voltammogram of $[NaFe(trop_2dad)(thf)_3]$ (**2**) at 23°C in 0.1 M solution of $[N(nBu)_4][PF_6]$ in THF; potential vs. Fc/Fc^+; working electrode: glassy carbon; counter electrode: Pt; reference electrode: Ag.

Trop$_2$dad. The ligand used in this work, trop$_2$dad, crystallizes in the monoclinic space group $P2_1/c$ with Z = 2. The diazadiene unit shows an *s-trans* conformation. Especially the bond lengths in the ligand backbone (C16–N1, C16–C16') and those of the olefin groups (C4–C5) are of interest (caption Figure S13). In the free ligand, these parameters are unexceptional.[20] Nevertheless, their accurate determination is important for comparison with compounds in which trop$_2$dad is bound to a metal center. In such cases, these parameters can give information about the oxidation state of the ligand (trop$_2$dad, (trop$_2$dad)$^{\bullet-}$, or (trop$_2$dad)$^{2-}$)[21,22] and about the strength of backbonding from the metal center to the olefin moieties.

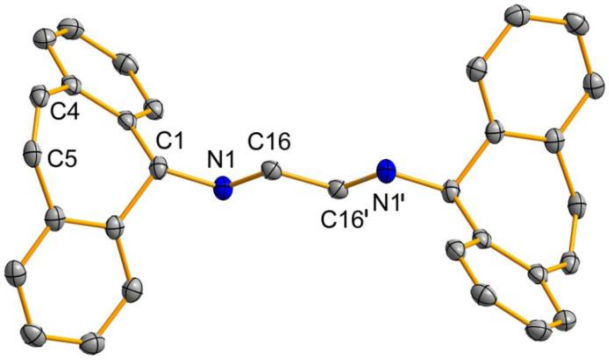

Figure S13. Molecular structure of trop$_2$dad in the solid state. Displacement ellipsoids are shown at the 50% probability level. Hydrogen atoms and one molecule of 1,2-dimethoxyethane per formula unit in the lattice are omitted for clarity. Selected bond lengths [Å]: C4–C5, 1.3362(19); C16–C16', 1.472(2); C1–N1, 1.4586(15); C16–N1, 1.2641(16).

[FeBr$_2$(trop$_2$dad)] (1). Compound **1** crystallizes in the monoclinic space group $P2_1/n$ with Z = 4 (Figure S14). The Fe center is found in a distorted tetrahedral coordination geometry.

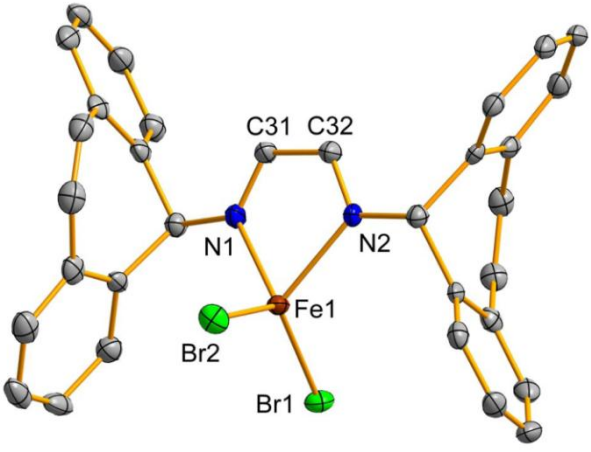

Figure S14. Molecular structure of [FeBr$_2$(trop$_2$dad)] (**1**) in the solid state. Displacement ellipsoids are shown at the 50% probability level. Hydrogen atoms and one molecule of toluene per formula unit in the lattice are omitted for clarity. Selected bond lengths [Å] and angles [°]: Fe1–N1, 2.1081(17); Fe1–N2, 2.1199(17); Fe1–Br1, 2.3689(4); Fe1–Br2, 2.3755(4); C31–N1, 1.276(3); C32–N2, 1.275(3); C31–C32, 1.480(3); N1–Fe1–N2, 78.19(7); N1–Fe1–Br1, 106.53(5); N1–Fe1–Br2, 113.87(5); N2–Fe1–Br1, 119.53(5); N2–Fe1–Br2, 99.82(5); Br1–Fe1–Br2, 128.197(15).

The N1–Fe1–N2 angle is small (78.19(7)°) due to geometric constraints of the chelating ligand. The largest angle around Fe is observed for Br1–Fe1–Br2 (128.197(15)°). The long C31–C32 bond (1.480(3) Å) and the short C31/C32–N1/N2 bonds (1.276(3) and 1.275(3) Å, respectively) are close to the values found in the non-coordinate ligand (*vide supra*) and indicate that the diazadiene ligand is in its neutral oxidation state, $(trop_2dad)^0$. Accordingly, the Fe1–N1/N2 distances (2.1081(17) and 2.1199(17) Å, respectively) are significantly elongated compared to those in compound **2** (1.8776(19) and 1.8793(19) Å, respectively). The Fe1–N1/N2 and Fe1–Br1/Br2 distances in **1** are highly similar to those reported for $[FeBr_2(tBu_2dad)]$.[23]

$[Fe(trop_2dad)_2]$ (4). Compound **4** crystallizes in the monoclinic space group *Pna2₁* with $Z = 4$ (Figure S15). The average Fe–N bond length of 1.992(3) Å is in the range of distances observed in related compounds $[Fe(RN\text{-}C_2\text{-}NR)_2]$ (R = C_6F_5, C_2 = $(MeC)_2$: 1.962(2) Å; R = Ph, C_2 = bornylene: 2.019(2) Å).[24] The dihedral angle between the two diazadiene planes amounts to 73.82(10)°, similar to the value of 73.0° reported for the bornylene compound. Fe1 resides in a distorted tetrahedral coordination geometry (N–Fe1–N, 82.88(10)-134.34(11)°). The C–C (1.372(4)-1.401(4) Å) and C–N (1.335(3)-1.347(3) Å) bond lengths in the diazadiene backbones reveal both ligands to be monoanionic radicals, $(trop_2dad)^{\bullet-}$. An effective magnetic moment of μ_{eff} = 2.6(1) μ_B was determined by Evans' method, which is close to the spin only value for two unpaired electrons (2.83 μ_B for $g = 2$). This suggests a high spin Fe(II) center (S_{Fe} = 2) antiferromagnetically coupled with the two radical ligands resulting in a spin ground state of S = 1. Mössbauer parameters of δ = 0.60(1) mm/s and $|\Delta E_Q|$ = 4.49(1) mm/s support this interpretation.[24a,25]

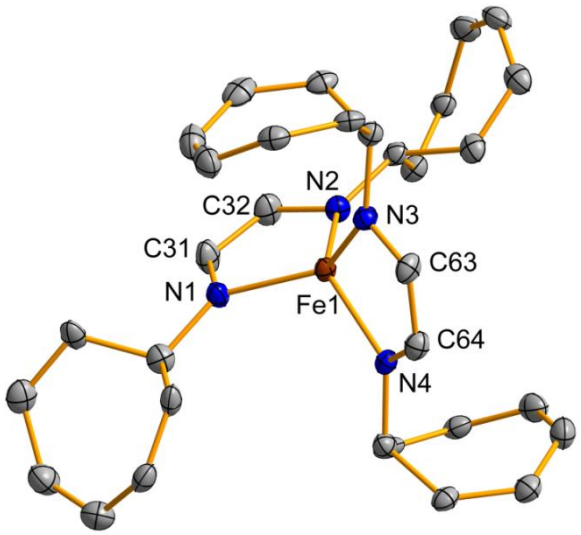

Figure S15. Molecular structure of $[Fe(trop_2dad)_2]$ (**4**) in the solid state. Displacement ellipsoids are shown at the 50% probability level. Hydrogen atoms, annelated C_6H_4 groups, and solvent molecules in the lattice are omitted for clarity. A second equivalent of **4** is present in the asymmetric unit and is not discussed as it shows highly similar bonding parameters. Selected bond lengths [Å] and angles [°]: Fe1–N1, 1.992(3); Fe1–N2, 1.991(3); Fe1–N3, 1.983(3); Fe1–N4, 2.001(3); C31–N1, 1.343(4); C32–N2, 1.343(4); C31–C32, 1.376(5); C63–N3, 1.339(4); C64–N4, 1.334(4); C63–C64, 1.398(5); N1–Fe1–N2, 84.53(11); N1–Fe1–N3, 134.34(11); N1–Fe1–N4, 115.20(11); N2–Fe1–N3, 116.25(11); N2–Fe1–N4, 130.45(10); N3–Fe1–N4, 82.88(10).

Reaction of [Na(thf)$_3$Fe(trop$_2$dad)] (2) with Ph$_3$CCl. In order to investigate the stability of the (Fe(trop$_2$dad))$^-$ anion in the presence of the potential oxidation agent (Ph$_3$C)$^+$, [Na(thf)$_3$Fe(trop$_2$dad)] (**2**) was reacted with one equivalent of Ph$_3$CCl (Scheme S1). Analyses of the products isolated from this reaction let us suggest two competing reaction pathways A and B. We propose the formation of intermediate **I-1** as the initial step common to both pathways.

Pathway A: Gomberg hydrocarbon **5** was isolated from the reaction mixture. **5** is the known dimerization product of the (Ph$_3$C)$^\bullet$ radical.[15] This indicates that *in situ* generated (Ph$_3$C)$^+$ indeed acts as an oxidizing agent. Surprisingly, [Fe$_3$(trop$_2$dad)$_2$] (**3**) was isolated as a second product. It is formally derived from three equivalents of transient (Fe(trop$_2$dad))$^-$ in a sequence involving three one electron oxidation steps and dissociation of neutral trop$_2$dad.

Pathway B: [Fe(trop$_2$dad-CPh$_3$)] (**6**) was isolated from this reaction in low yield. It is a formal adduct of radical species (Ph$_3$C)$^\bullet$ and (Fe(trop$_2$dad))$^\bullet$. However, the connectivity in the diazadiene backbone shows that a subsequent rearrangement involving H-migration has taken place. Additions to diazadiene backbones have been reported for Zr, Hf,[26a] Ta,[26b] and Ln[26c] (Ln = Sc, Y, Lu) species and have been shown to be radical reactions in case of Ta.[26b]

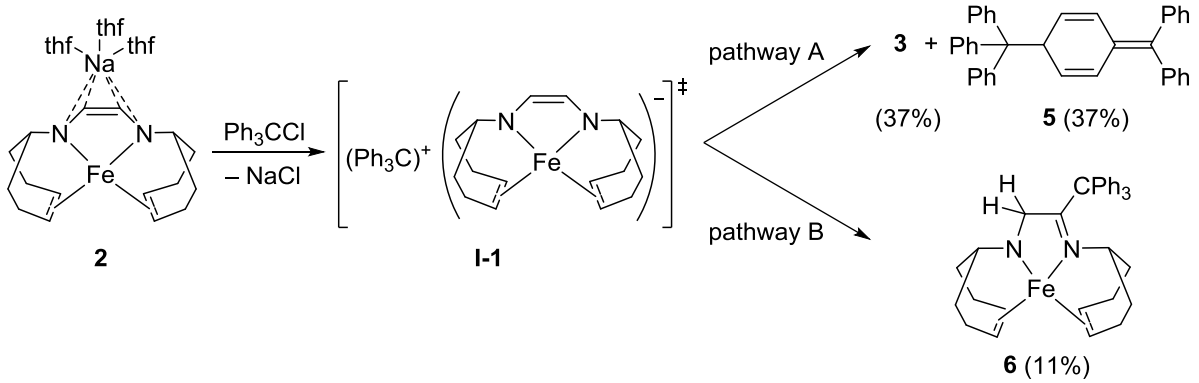

Scheme S1. Reaction of **2** with Ph$_3$CCl to give **3** and **5** (pathway A) and **6** (pathway B).

Ph$_3$CC$_6$H$_5$CPh$_2$ (5). Structures of Ph$_3$CC$_6$H$_5$CPh$_2$ with different or without solvent molecules in the lattice have previously been reported.[27] **5** contains one molecule of hexanes per Ph$_3$CC$_6$H$_5$CPh$_2$ in the lattice. Bond lengths and angles of the actual molecule do not differ significantly (Figure S16).

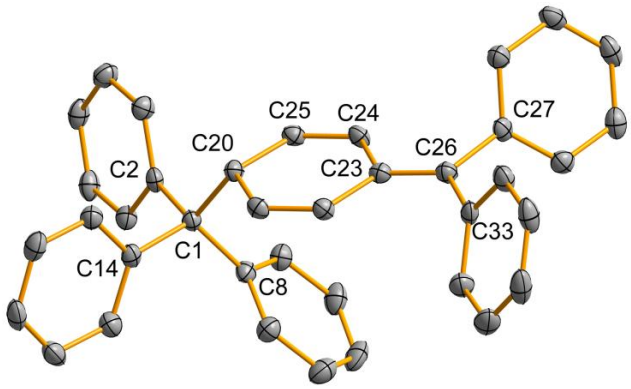

Figure S16. Molecular structure of [(Ph$_3$C(C$_6$H$_5$)CPh$_2$) · (Hexanes)] (**5**) in the solid state. Hydrogen atoms and one molecule of hexanes per asymmetric unit are omitted for clarity. Displacement ellipsoids are shown at the 50% probability level.

[Fe(trop$_2$dad-CPh$_3$)]·(Tol) (6). 6 crystallizes in the triclinic space group P with Z = 2 (Figure S17). The iron center is coordinated by two N-functionalities and two olefinic moieties. It resides in a distorted square planar coordination geometry with an angle sum of 364.65(7)° around Fe (N/C–Fe1–N/C, 81.54(6)-98.04(8)°). The NCCN backbone of the ligand displays one long C31–N1 bond (1.368(2) Å) and one short C32–N2 bond (1.3283(19) Å), which are associated with an amido and an imino functionality, respectively.[28] This is in good agreement with a short Fe1–N1 distance (1.8653(13) Å) and a large Fe1–N2 distance (1.9446(15) Å). However, these differences in Fe–N bonding do not induce a thermodynamic *trans*-effect in **6**, as the Fe–olefin bond lengths are identical within limits of error (and elongated compared to **2**). The C31–C32 distance of 1.446(3) Å indicates single bond character. Accordingly, C32 shows a planar coordination geometry (Σ°, 359.97(14)°). Thus, compound **6** contains a monoanionic amido-imino diolefin ligand. An effective magnetic moment of μ_{eff} = 1.6 μ_B was determined for **6** using Evans' method. This is close to the spin only value of one unpaired electron (1.73 μ_B for g = 2) and suggests an Fe(I) l.s. electron configuration.

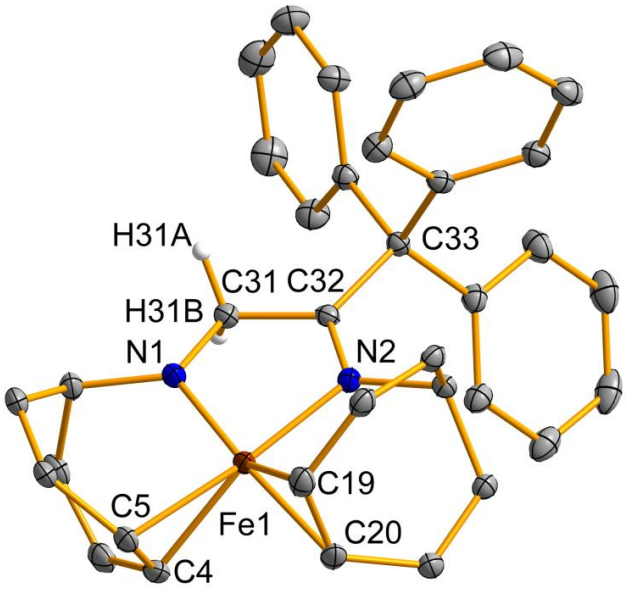

Figure S17. Molecular structure of **6** in the solid state; displacement ellipsoids are shown at the 50% probability level; hydrogen atoms are omitted for clarity, except for H31A/B, which are shown as arbitrary spheres. Selected bond lengths [Å] and angles [°]: Fe1–N1, 1.8647(15); Fe1–N2, 1.9438(14); Fe1–(C4–C5), 1.9360(18); Fe1–(C19–C20), 1.9361(18); C4–C5, 1.419(3); C19–C20, 1.426(3); C31–C32, 1.445(2); C32–C33, 1.547(2); C31–N1, 1.369(2); C32–N2, 1.328(2); N1–Fe1–N2, 81.57(6); N1–Fe1–(C4–C5), 91.67(7); N1–Fe1–(C19–C20), 161.86(7); N2–Fe1–(C4–C5), 161.41(7); N2–Fe1–(C19–C20), 93.37(7); (C19–C20)–Fe1–(C4–C5), 98.03(7); Σ(C31/C33/N2–C32–C33/N2/C31), 359.97(14).

Theoretical Calculations, [NaFe(trop$_2$dad)(thf)$_3$] (2). The DFT calculated Mössbauer parameters of [NaFe(trop$_2$dad)(thf)$_3$] (**2**) are in reasonable agreement with the experimental parameters (Table S2). The absolute values of the computed isomer shifts (DFT: δ = 0.23-0.28 mm/s) are only slightly overestimated (exp: δ = 0.21 mm/s). However, the computed quadrupole splitting (DFT: ΔE_Q = 1.58-1.77 mm/s) are somewhat underestimated (exp: $|\Delta E_Q|$= 2.45(1) mm/s). This is not caused by small differences in the X-ray coordination geometries compared to the optimized geometries in the gas phase, as the DFT calculated Mössbauer parameters are similar when the X-ray geometries are used without any prior geometry optimization (Table S2). We thus speculate that the experimental Mössbauer parameters are influenced by electrostatic forces and/or weak intermolecular exchange interactions between the [Fe(trop$_2$dad)]$^-$ anions in the solid state. Alternatively, the Mössbauer parameters might not be predicted accurately enough by the applied DFT methods.

***Table S2*.** Experimental and DFT calculated Mössbauer parameters[(a), (b)]

Exp.	ρ[(c)]	δ, mm/s [(d)]	ΔE_Q, mm/s
[NaFe(trop$_2$dad)(thf)$_3$] (**2**)	-	0.21(1)	2.45(1)
DFT [(a), (b)]	ρ[(c)]	δ, mm/s [(d)]	ΔE_Q, mm/s
[Fe(trop$_2$dad)]$^-$	*11582.91935*	*0.248*	*1.581*
[NaFe(trop$_2$dad)]	*11582.81022*	*0.281*	*1.673*
[NaFe(trop$_2$dad)(thf)$_3$] *DFT geom.*	*11582.84025*	*0.272*	*1.678*
[NaFe(trop$_2$dad)(thf)$_3$] *X-ray geom. assym. unit 1* [(e)]	*11582.90528*	*0.252*	*1.733*
[NaFe(trop$_2$dad)(thf)$_3$] *X-ray geom. assym. unit 2* [(e)]	*11582.9572*	*0.237*	*1.773*

(a) Geometries optimized with Turbomole (BP86, def2-TZVP).

(b) Mössbauer parameters calculated with Orca (b3-lyp, TZVP) using the Turbomole optimized geometries.

(c) Calculated total electron density at the iron nucleus.

(d) Isomer shift $\delta = \alpha\,(\rho - C) + \beta$, with α = –0.298, β = 1.118 and C = 11580.[29]

(e) Geometry found in the X-ray structure, not optimized with DFT.

[$Fe_3(trop_2dad)_2$] (3). Four electronic states of **3** were calculated by DFT methods using the experimentally determined crystal structure: S = 1 (**3**^{A}), S = 2 (**3**^{B}), S = 3 (**3**^{C}) and S = 5 (**3**^{D}) corresponding to *ls*-Fe(I)–*hs*-Fe(II)–*ls*-Fe(I) (**3**^{A}: antiferromagnetic spin arrangement; **3**^{B}: mixed spin arrangement; **3**^{C}: ferromagnetic spin arrangement) and *hs*-Fe(I)–*hs*-Fe(II)–*hs*-Fe(I) (**3**^{D}) electronic configurations. Fe localized Löwdin spin densities in **3** are highly similar when calculated using the TZVP or the CP(PPP) basis sets for Fe. The spin density at the central iron ion is 3.39-3.67 confirming the *hs*-Fe(II) local state in all considered compounds **3**$^{A-D}$ (Table S3). The covalent $Fe^{central}$–N interactions are responsible for the slightly decreased spin density at the metal ion compared with the theoretical value 4.00. The absolute value of the spin density at each terminal iron ion is in average 0.98-1.15 for **3**$^{A-C}$ and 2.96-2.97 for **3**^{D}, respectively. These values are in agreement with *ls*-Fe(I) and *hs*-Fe(I) local states in **3**$^{A-C}$ and **3**^{D}, respectively. Enhanced spin-polarization and possibly also increased covalent $Fe^{central}$–$Fe^{terminal}$ interactions lead to the higher than expected (1.00) spin density at terminal iron ions in **3**^{B,C}.

The Mössbauer parameters were calculated with density functional theory calculations for **3**$^{A-D}$. For all four spin states, the computed isomer shifts δ are in reasonable agreement with the experimentally determined values (Tables S4, S5). However, the calculated isomer shift values for **3**^{A}-**3**^{D} are too similar to allow for a reliable distinction between the spin states of **3**$^{A-D}$. I. e. an unambiguous electronic structure determination of **3** is not possible by only comparing calculated (TZVP or CP(PPP) basis set) with experimentally determined Mössbauer parameters.

Table S3. Fe localized Löwdin spin density for **3** obtained from spin-unrestricted DFT Orca calculations (b3-lyp/TZVP and B3LYP/CP(PPP)).

Basis set for Fe	Fe1 (terminal)		Fe2 (central)		Fe3 (terminal)		$<S^2>$	
	TZVP	CP(PPP)	TZVP	CP(PPP)	TZVP	CP(PPP)	TZVP	CP(PPP)
S = 5	2.96	2.97	3.65	3.67	2.96	2.97	30.3	30.3
S = 3	1.14	1.16	3.65	3.67	1.13	1.14	12.1	12.1
S = 2	1.15	-	3.51	-	-0.97	-		-
S = 1	-0.98	-	3.39	-	-0.97	-		-

Table S4. Mössbauer parameters for $\mathbf{3^{A-D}}$ obtained from spin-unrestricted DFT b3-lyp/TZVP calculations and experimentally determined values.

		Compound 3^{A} (S = 1)	**Compound 3^{B} (S = 2)**	**Compound 3^{C} (S = 3)**	**Compound 3^{D} (S = 5)**	**Exp.**
Basis set for Fe		TZVP	TZVP	TZVP	TZVP	
Fe1^{terminal}	δ, mm/s	+0.49 [a]	+0.50 [a]	+0.50 [a]	+0.56 [a]	+0.37(1)
	ΔE_Q, mm/s	–0.665	+0.80	+0.79	–1.07	1.09(1)[d]
	η[c]	0.753	0.524	0.50	0.46	-
Fe3^{terminal}	δ, mm/s	+0.49 [a]	+0.49 [a]	+0.50 [a]	+0.56 [a]	+0.37(1)
	ΔE_Q, mm/s	–0.632	–0.625	+0.77	–1.08	1.09(1)[c]
	η[c]	0.378	0.391	0.58	0.62	-
Fe2^{central}	δ, mm/s	+0.77 [a]	+0.78 [a]	+0.80 [a]	+0.80 [a]	+0.92(1)
	ΔE_Q, mm/s	+2.868	+2.938	+2.07	+1.88	1.88(1)[c]
	η[c]	0.545	0.678	0.77	0.58	-

[a] Isomer shift $\delta = \alpha\,(\rho - C) + \beta$, with α = –0.298, β = 1.118 and C = 11580.[29]
[c] Asymmetry parameter $\eta = (V_{xx}–V_{yy})/V_{zz}$ ($0 \le \eta \le 1$).
[d] The sign is not determined experimentally.

Table S5. Mössbauer parameters for $\mathbf{3^{C,D}}$ obtained from spin-unrestricted DFT calculations (b3-lyp/TZVP and B3LYP/CP(PPP)) and experimentally determined values.

		Compound 3^{C} (S = 3)		**Compound 3^{D} (S = 5)**		**Exp.**
Basis set for Fe		TZVP	CP(PPP)	TZVP	CP(PPP)	
Fe1^{terminal}	δ, mm/s	+0.50 [a]	+0.41 [b]	+0.56 [a]	+0.47 [b]	+0.37(1)
	ΔE_Q, mm/s	+0.79	+0.91	–1.07	–1.18	1.09(1)[d]
	η[c]	0.50	0.47	0.46	0.41	-
Fe3^{terminal}	δ, mm/s	+0.50 [a]	+0.41 [b]	+0.56 [a]	+0.48 [b]	+0.37(1)
	ΔE_Q, mm/s	+0.77	+0.89	–1.08	–1.20	1.09(1)[c]
	η[c]	0.58	0.64	0.62	0.54	-
Fe2^{central}	δ, mm/s	+0.80 [a]	+0.73 [b]	+0.80 [a]	+0.73 [b]	+0.92(1)
	ΔE_Q, mm/s	+2.07	+2.83	+1.88	+2.43	1.88(1)[c]
	η[c]	0.77	0.28	0.58	0.18	-

[a] Isomer shift $\delta = \alpha\,(\rho - C) + \beta$, with α = –0.298, β = 1.118 and C = 11580.[29]
[b] Isomer shift $\delta = \alpha\,(\rho - C) + \beta$, with α = –0.36662, β = 6.45806 and C = 11800.[13]
[c] Asymmetry parameter $\eta = (V_{xx}–V_{yy})/V_{zz}$ ($0 \le \eta \le 1$).
[d] The sign is not determined experimentally.

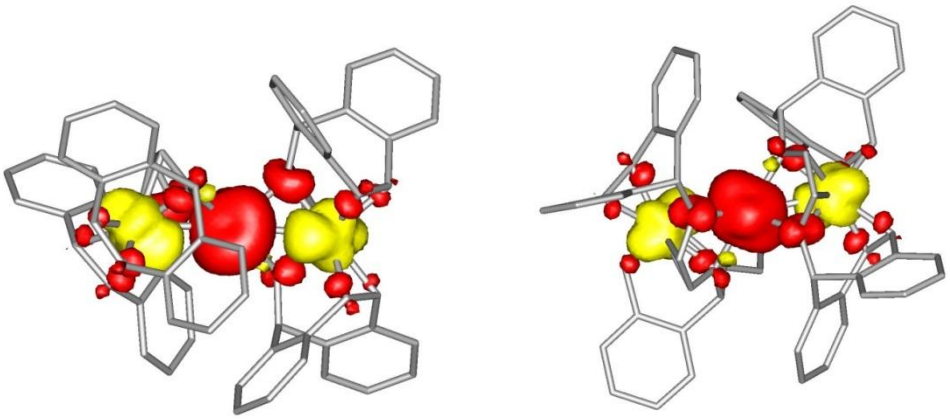

Figure S18. Spin density for **3**$^{\mathbf{A}}$ obtained from spin-unrestricted B3LYP-DFT calculations, *S* = 1 state (*ls*-Fe^{I}–*hs*-Fe^{II}–*ls*-Fe^{I}; antiferromagnetic arrangement). Red: positive spin density (excess α-spin density); Yellow: Negative spin density (excess β-spin density). Löwdin spin density values shown in Table S3.

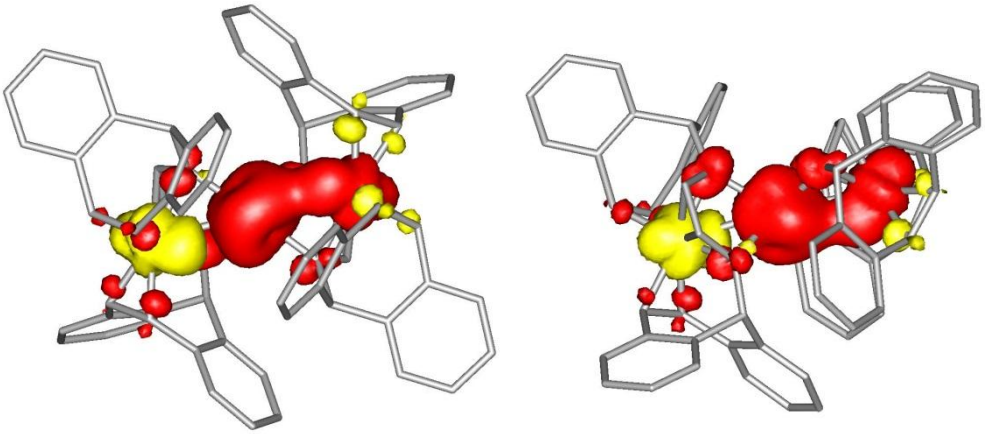

Figure S19. Spin density for **3**$^{\mathbf{B}}$ obtained from spin-unrestricted B3LYP-DFT calculations (TZVP basis set for Fe), *S* = 2 state (*ls*-Fe^{I}–*hs*-Fe^{II}–*ls*-Fe^{I}; mixed spin arrangement). Red: positive spin density (excess α-spin density); Yellow: Negative spin density (excess β-spin density). Löwdin spin density values shown in Table S3.

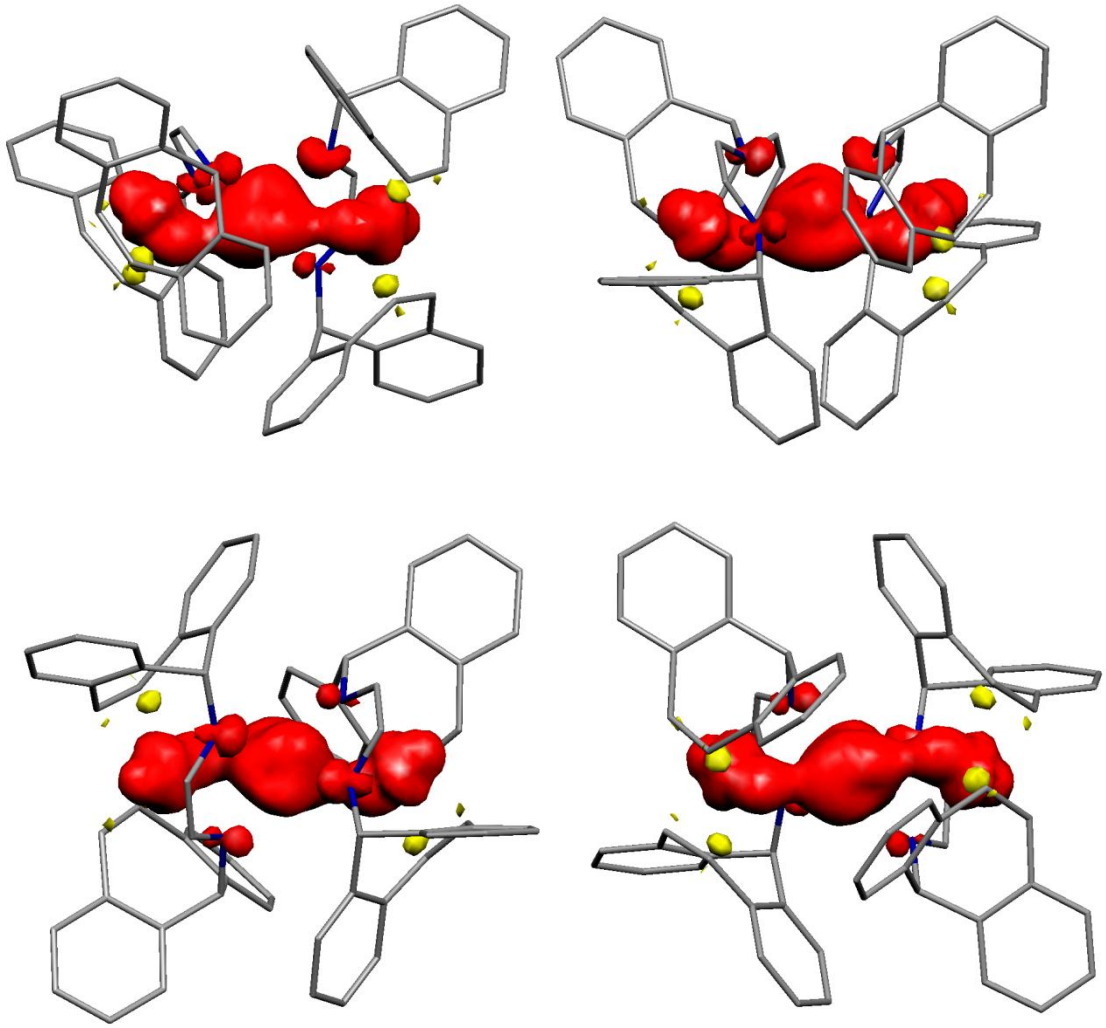

Figure S20. Spin density for $\mathbf{3^C}$ obtained from spin-unrestricted B3LYP-DFT calculations (CP(PPP) basis set for Fe), S = 3 state (*ls*-Fe^{I}–*hs*-Fe^{II}–*ls*-Fe^{I}).

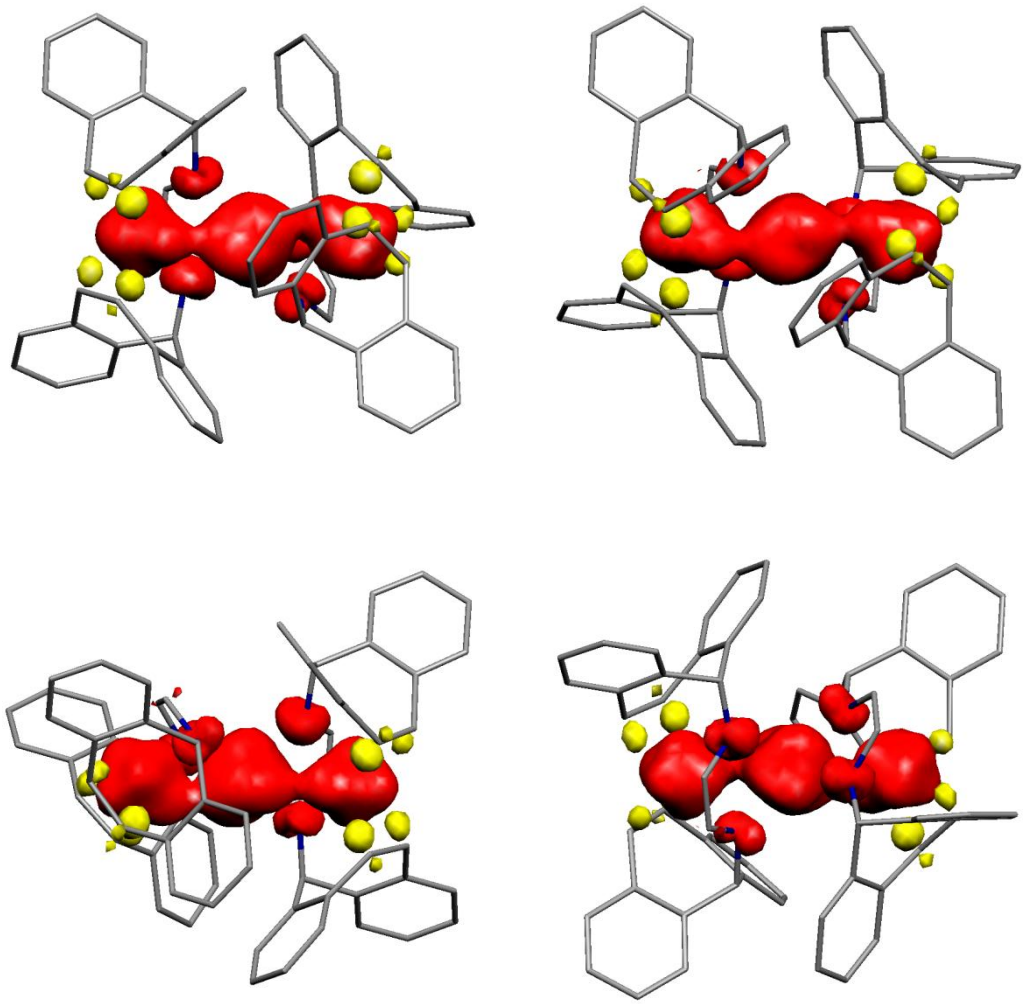

Figure S21. Spin density for **3^{D}** obtained from spin-unrestricted B3LYP-DFT calculations (CP(PPP) basis set for Fe), S = 5 state (*hs*-Fe^{I}–*hs*-Fe^{II}–*hs*-Fe^{I}).

References.

1 R. Ahlrichs, Turbomole Version 6.5, Theoretical Chemistry Group, University of Karlsruhe.

2 PQS version 2.4, 2001, Parallel Quantum Solutions, Fayettevile, Arkansas (USA); the Baker optimizer is available separately from PQS upon request: I. Baker, *J. Comput. Chem.*, 1986, **7**, 385.

3 P. H. M. Budzelaar, *J. Comput. Chem.*, 2007, **28**, 2226-2236.

4 M. Sierka, A. Hogekamp, R. Ahlrichs, *J. Chem. Phys.* 2003, **118**, 9136.

5 (a) A. D. Becke, *Phys. Rev. A*, 1988, **38**, 3098. (b) J. P. Perdew, *Phys. Rev. B*, 1986, **33**, 8822.

6 (a) F. Weigend, R. Ahlrichs, *Phys. Chem. Chem. Phys.* 2005, **7**, 3297–3305; (b) F. Weigend, M. Häser, H. Patzelt, R. Ahlrichs, *Chem. Phys. Lett.*, 1998, **294**, 143.

7 Neese, F. ORCA – An ab initio, Density Functional and Semiempirical program package, Version 3.0.2. Max-Planck-Insitut für Bioanorganische Chemie, Mülheim and der Ruhr, 2009.

8 (a) C. Lee, W. Yang, R. G. Parr, *Phys. Rev. B*, 1988, **37**, 785; (b) A. D. Becke, *J. Chem. Phys.* **1993**, *98*, 1372; (c) A. D. Becke, *J. Chem. Phys.*, 1993, **98**, 5648; (d) Calculations were performed using the "Turbomole functional b3-lyp", which is not completely identical to the "Gaussian B3LYP functional".

9 F. Neese, *ORCA – an Ab Initio, Density Functional and Semiempirical SCF-MO Package*, version 2.7 revision 0; Institut für Physikalische und Theoretische Chemie, Universität Bonn, Germany, 2009.

10 A. D. Becke, *J. Chem. Phys.* 1993, **98**, 5648.

11 The ORCA basis set 'CoreProp' was used. This basis is based on the TurboMole DZ basis developed by Ahlrichs and coworkers and obtained from the basis set library under *ftp.chemie.uni-karlsruhe.de/pub/basen.*

12 A. Schäfer, H. Horn, R. Ahlrichs, *J. Chem. Phys.* 1992, **97**, 2571.

13 (a) F. Neese, *Inorg. Chim. Acta* 2002, **337**, 181; (b) S. Sinnecker, L. D. Slep, E. Bill, F. Neese, *Inorg. Chem.* 2005, **44**, 2245.

14 S. Portmann, *Molekel*, version 4.3.win32; CSCS/UNI Geneva, Switzerland, 2002.

15 H. Volz, W. Lotsch, H.-W. Schnell, *Tetrahedron*, 1970, **26**, 5343.

16 We use the term microcrystalline here to describe material composed of a large number of small single crystals (size in the range of ca. $(0.1\text{-}0.5\ \text{mm})^3$).

17 Other iron based trinuclear clusters showed a field dependent magnetic moment, see: J. J. Girerd, G. C. Papaefthymiou, A. D. Watson, E. Gamp, K. S. Hagen, N. Edelstein, R. B. Frankel, R. H. Holm, *J. Am. Chem. Soc.*, 1984, **106**, 5941.

18 Long-range intermolecular magnetic interactions in solid **3** or single molecule magnet characteristics of **3** could in principle contribute to this behavior. The latter option seems unlikely at this stage as it would require a high spin electron configuration of the terminal Fe ions, for which a fit of the magnetic susceptibility data gave extremely unusual values (spin coupling model for a spin triad of isosceles topology with $S_{Fe1} = S_{Fe3} = 3/2$, $S_{Fe2} = 2$ gave $g_{Fe1} = g_{Fe3} < 1.5$; $|D_{Fe1}| = |D_{Fe3}| > 1700\ \text{cm}^{-1}$).

19 E.g.: (a) G. Vázquez-Victorio, U. Acevedo-Salas, R. Valenzuela, *Microwave Absorption in Nanostructured Spinel Ferrites* in *Ferromagnetic Resonance - Theory and Applications*, ed.: O. Yalcin, 2013; (b) C. Carbone, F. Di Benedetto, P. Marescotti, C. Sangregorio, L. Sorace, N. Lima, M. Romanelli, G. Lucchetti, and C. Cipriani, *Mineralogy and Petrology*, 2005, **85**, 19; (c) M. M. Noginov, N. Noginova,

O. Amponsah, R. Bah, R. Rakhimov, V. A. Atsarkin, *J. Magn. Magn. Mater.*, 2008, **320**, 2228.

20 (a) F. Stoffelbach, R. Poli, S. Maria, P. Richard, *J. Organomet. Chem.*, 2007, **692**, 3133; (b) J. Keijsper, H. van der Poel, L. H. Polm, G. van Koten, K. Vrieze, P. F. A. B. Seignette, R. Varenhorst, C. Stam, *Polyhedron*, 1983, **2**, 1111; (c) S. Anga, R. K. Kottalanka, T. Pal, T. K. Panda, *J. Mol. Struct.*, 2013, **1040**, 129.

21 M. M. Khusniyarov, T. Weyhermüller, E. Bill, K. Wieghardt, *J. Am. Chem. Soc.*, 2009, **131**, 1208.

22 (a) J. Liedtke, S. Loss, C. Widauer, H. Grützmacher, *Tetrahedron*, 2000, **56**, 143; (b) J. R. Rodgers, O. Kennard, G. M. Sheldrick, A. S. Horn, *Acta Cryst*., 1976, **B32**, 1293; (c) E. V. Banide, C. O'Connor, N. Fortune, Y. Ortin, S. Milosevic, H. Müller-Bunz, M. J. McGlinchey, *Org. Biomol. Chem.* 2010, **8**, 3997.

23 R. K. O'Reilly, M. P. Shaver, V. C. Gibson, A. J. P. White, *Macromolecules*, 2007, **40**, 7441.

24 (a) M. M. Khusniyarov, T. Weyhermüller, E. Bill, K. Wieghardt, *J. Am. Chem. Soc.*, 2009, **131**, 1208; (b) N. Muresan, C. C. Lu, M. Ghosh, J. C. Peters, M. Abe, L. M. Henling, T. Weyhermöller, E. Bill, K. Wieghardt, *Inorg. Chem*., 2008, **47**, 4579.

25 The sample used for Mössbauer spectroscopy was prepared using an alternative protocol (Na as a reducing agent) and contained impurities identified as **2** and tentatively assigned to a species [Fe($trop_2$dad)$(L)_n$] (L = neutral ligand, n = 0-2). Mössbauer data: component 1 (62%, **4**): δ = 0.60(1) mm/s, $|\Delta E_Q|$ = 4.49(1) mm/s, Γ_{FWHM} = 0.30(1) mm/s; component 2 (7%, **2**): δ = 0.23(1) mm/s, $|\Delta E_Q|$ = 2.52(1) mm/s, Γ_{FWHM} = 0.29(1) mm/s; component 3 (31%, [Fe($trop_2$dad)$(L)_n$]): δ = 0.40(1) mm/s, $|\Delta E_Q|$ = 1.51(1) mm/s, Γ_{FWHM} = 0.85(1) mm/s.

26 (a) P. De Waele, B. A. Jazdzewski, J. Klosin, R. E. Murray, C. N. Theriault, P. C. Vosejpka, J. L. Petersen, *Organometallics*, 2007, **26**, 3896; (b) H. Tsurugi, T. Saito, H. Tanahashi, J. Arnold, K. Mashima, *J. Am. Chem. Soc.*, 2011, **133**, 18673; (c) G. Du, Y. Wei, L. Ai, Y. Chen, Q. Xu, X. Liu, S. Zhang, Z. Hou, X. Li, *Organometallics*, 2011, **30**, 160.

27 (a) N. S. Blom, G. Roelofsen, J. A. Kanters, *Cryst. Struct. Commun.*, 1982, **11**, 297; (b) J. Allemand, R. Gerdil; *Acta Crystallogr. B,* 1978, **34**, 2214; (c) L. N. Bochkarev, N. E. Molosnova, L. N. Zakharov, G. K. Fukin, A. I. Yanovsky, Y. T. Struchkov; *Acta Crystallogr.C*, 1995, **51**, 489.

28 The C31–N1 distance is shorter than in other compounds with amido-imino ligands (ca. 1.45 Å, see ref. 26). Thus, a ligand backbone (NCHCCPh_3N) was considered for **6** (monoanionic, delocalized radical). However, this possibility was ruled out as C–C and C–N bond distances in the ligand backbone of **6** disagree with those found in the literature for a Ni complex with asymmetric, monoanionic radical diazadiene ligands: N. Muresan, K. Chlopek, T. Weyhermüller, F. Neese, K. Wieghardt, *Inorg. Chem.*, 2007, **46**, 5327.

29 M. Römelt, S. Ye, F. Neese, *Inorg. Chem*., 2009, **48**, 784.